



A Mem-dELISA platform for dual color and ultrasensitive digital detection of colocalized proteins on extracellular vesicles

Himani Sharma ^{a,1}, Vivek Yadav ^{a,1}, Alice Burchett ^b, Tiger Shi ^a, Satyajyoti Senapati ^a, Meenal Datta ^b, Hsueh-Chia Chang ^{a,b,*}

^a Department of Chemical and Biomolecular Engineering, University of Notre Dame, Notre Dame, IN, 46556, USA

^b Department of Aerospace and Mechanical Engineering, University of Notre Dame, Notre Dame, IN, 46556, USA



ARTICLE INFO

Keywords:
 Digital immunoassay
 Protein colocalization
 Multiplex digital ELISA
 Extracellular vesicles
 Dual color enzyme

ABSTRACT

Accurate, multiplex, and ultrasensitive measurement of different colocalized protein markers on individual tumor-derived extracellular vesicles (EVs) and dimerized proteins with multiple epitopes could provide insights into cancer heterogeneity, therapy management and early diagnostics that cannot be extracted from bulk methods. However, current digital protein assays lack certain features to enable robust colocalization, including multi-color detection capability, large dynamic range, and selectivity against background proteins. Here, we report a lithography-free, inexpensive (< \$0.1) and ultrasensitive dual-color Membrane Digital ELISA (Mem-dELISA) platform by using track-etched polycarbonate (PCTE) membranes to overcome these shortcomings. Their through-pores remove air bubbles through wicking before they are sealed on one side by adhesion to form microwells. Immunomagnetic bead-analyte complexes and substrate solution are then loaded into the microwells from the opposite side, with >80% loading efficiency, before sealing with oil. This enables duplex digital protein colorimetric assay with beta galactosidase and alkaline phosphatase enzymes. The platform achieves 5 logs of dynamic range with a limit of detection of 10 aM for both Biotinylated β -galactosidase (B- β G) and Biotin Alkaline Phosphatase Conjugated (B-ALP) proteins. We demonstrate its potential by showing that a higher dosage of paclitaxel suppresses EpCAM-positive EVs but not GPC-1 positive EVs from breast cancer cells, a decline in chemo-resistance that cannot be detected with Western blot analysis of cell lysate. The Mem-dELISA is poised to empower researchers to conduct ultrasensitive, high throughput protein colocalization studies for disease diagnostics, treatment monitoring and biomarker discovery.

1. Introduction

Breast cancer is one of the leading malignancies among women in the United States, ranking second in cancer-related deaths. Despite recent advances in diagnostics and therapy monitoring, such as mammography, magnetic resonance imaging (MRI), and whole-breast ultrasonography, high false positive results limit their effectiveness (Kelly et al., 2010; Roganovic et al., 2015). Moreover, invasive procedures such as tissue biopsies suffer from extended turnaround times, operator bias, and potential misinterpretations owing to tumor heterogeneity, thus making them incompatible for tumor monitoring during treatment with anticancer drugs (Alba-Bernal et al., 2020). In contrast, liquid biopsy offers a promising alternative by analyzing a wide array of proteins and genes present in biofluids like blood, saliva, or urine (Connal et al.,

2023). These molecular biomarkers are often carried by nanocarriers like lipoproteins and Extracellular Vesicles (EVs). Hence, multiplex detection of different colocalized proteins that are markers of tissues of origin, cancer, drug-resistance, or metastasis on the same nanocarriers will provide more specific information about the disease. Therefore, rapid advancements have been made in quantifying several colocalized biomarkers on individual nanocarriers, like lipoproteins and tumor-derived EVs, present in a small volume of physiological fluids. These advances hold promise for early disease diagnostics, prognosis, and therapy management in patients (Cohen and Walt, 2019; Hinestrosa et al., 2022; Kelley et al., 2014; Landegren and Hammond, 2021; Rissin et al., 2010; Wu et al., 2020).

The current state-of-the-art technique for protein detection is Enzyme-Linked Immunosorbent Assay (ELISA) which suffers from the

* Corresponding author. Department of Chemical and Biomolecular Engineering, University of Notre Dame, Notre Dame, IN, 46556, USA.

E-mail address: hchang@nd.edu (H.-C. Chang).

¹ equal contributions.

<https://doi.org/10.1016/j.bios.2024.116848>

Received 18 March 2024; Received in revised form 29 July 2024; Accepted 9 October 2024

Available online 10 October 2024

0956-5663/© 2024 Elsevier B.V. All rights are reserved, including those for text and data mining, AI training, and similar technologies.

insufficient limit of detection (\sim nM-pM) beyond which several clinically relevant protein biomarkers (\sim pM-fM) of cancer remain undetected (Wu et al., 2022). To surpass this limitation, single-molecule arrays (Simoa) have been developed in which a protein molecule is sandwiched between an antibody coated magnetic beads and enzyme conjugated detection antibody to form an immunocomplex (Chang et al., 2012; Rivnak et al., 2015). Subsequently, the immunocomplex is sampled into thousands of femtoliter (fL) reaction chambers keeping the total protein concentration within the Poisson limit such that each bead contains either one or zero molecules. The fluorescence signal generated from the enzymatic reaction gives a digital readout providing an absolute quantification of the protein biomarker, circumventing any bias that usually occurs in other analog sensors based on current or voltage measurements. For the digital quantification of proteins, the focus has been on the fabrication of small microwell-based picoliter reactors, as the enzymatic reaction in ELISA has a linear amplification rate. The ultrasmall volume of a reactor enhances the localized concentration of fluorescent products which can be subsequently detected by a standard fluorescence microscope. Several other methods have been reported in the literature apart from Simoa for digital assay (Rondelez et al., 2005; Sakakihara et al., 2010; Shim et al., 2013; Witters et al., 2013).

Digital protein amplification assays face significant technical and practical challenges. Firstly, the sensor's dynamic range is directly influenced by the number of microwells in the device, dictated by a hard-to-modify master mold, thus hindering the biosensors' suitability for massive multiplexing applications. Moreover, the microwell fabrication itself requires complex and expensive cleanroom-based micro-fabrication techniques, further elevating the overall expense. Secondly, these assays necessitate expensive, bulky fluidic control apparatus like syringe pumps and centrifuges, and the frequent issue of air bubble entrapment in microwells complicates accurate quantification, often requiring bulky vacuum pumps and expensive surface treatments to resolve (Zandi Shafagh et al., 2019). Lastly and most importantly, Simoa-based multiplex assays have consistently employed color coding of magnetic beads and utilization of a single enzyme (beta-galactosidase) amplification reaction, which results in a maximum of 3-plex immunoassay in a single experimental run (Rissin et al., 2013; Wilson et al., 2016). The absence of multi-color digital ELISA enzymatic amplification makes this assay unsuitable for applications involving protein colocalization assay on EVs, lipoproteins, viruses, and proteins having multiple epitopes where the goal is to analyze multiple protein signatures on a single EV captured in a single microwell. Understandably, reports analyzing multiple proteins on EVs using digital ELISA have been performed by repeatedly changing the reporter antibody one at a time (Morasso et al., 2022; Wei et al., 2020).

To overcome the aforementioned challenges, we report a lithography-free, user-friendly, and inexpensive Mem-dELISA digital protein detection platform. The platform utilizes low-cost ($<$ \$0.1 material cost) disposable track-etched polycarbonate (PCTE) membranes. The membrane allows reagent loading by wicking through their pores (\sim 5 μ m) before they are adhered to a sticky surface to form thousands of picolitre microwells without generating any air bubbles. The Mem-dELISA platform was optimized to perform dual color digital enzymatic reaction of free-floating beta-galactosidase and alkaline phosphatase enzymes simultaneously. Magnetic beads were utilized to efficiently capture free floating protein molecules from the sample, with bead loading efficiency into the microwells optimized ($>$ 80%) with a permanent magnet and mechanical shaking. The Mem-dELISA digital protein detection biosensor obtained 5 logs of dynamic range (1 pM-10 aM) for both beta-galactosidase and alkaline phosphate enzymatic amplification with a limit of detection of 10 aM. As a proof-of-concept demonstration, we employed the digital biosensor to perform GPC-1 and EpCAM protein colocalization studies on EVs derived from paclitaxel drug-treated triple-negative breast cancer cell lines (MDA-MB-231 and MDA-MB-468). The study shows that increasing paclitaxel drug dosages resulted in a decrease in the fraction of EVs with colocalized

EpCAM-GPC-1 and a decrease in the fraction of EVs expressing EpCAM compared to untreated controls. These trends are not detectable from Western blots of cell lysate. This result clearly suggests the loss of chemo-resistance of cancer cells at high drug dosage, as a decrease in EpCAM expression on EVs has been correlated to loss of metastases and increased survival following drug treatment (Ali et al., 2019; Liu et al., 2019). Additionally, we believe that the user-friendly Mem-dELISA platform's facile setup, clean room fabrication free microwells formation, low consumables cost ($<$ \$0.1) as compared to typical microfluidics chips (\sim \$10), automatic air bubble removal, extremely low instrument cost (compared to $>$ \$100k of commercial digital ELISA platforms) and simplified workflows does not require an extensive amount of expertise which present a bottleneck for using them for point-of-care applications in resource-limited areas where usually a disposable sensor is preferred and expertise may be limited. This platform holds promise for advancing protein detection technologies, and improving diagnostics and therapy monitoring in various biomedical applications.

2. Materials and methods

2.1. Reagents and materials

Biotinylated β -galactosidase (B- β G) and Biotin Alkaline Phosphatase Conjugated (B-ALP) were purchased from Rockland Immunochemicals (PA, USA). Dynabeads M-280 Streptavidin, DynabeadsTM, Biotin conjugated CD326 (EpCAM) monoclonal antibody, RIPA buffer, and EppendorfTM LoBind microcentrifuge tubes were purchased from Thermo Fisher Scientific (MA, USA). Track-etched polycarbonate membranes were purchased from Sigma Aldrich (St. Louis, MO, USA) and Sterlitech Corporation (WA, USA). Resorufin β -D-Galactopyranoside (RDG), Fluorescein di(β -D-galactopyranoside) (FDG), streptavidin- β -galactosidase (S- β G), Biotin Alkaline Phosphatase Conjugated (S-ALP), Tween-20, Bovine Serum Albumin (BSA) and silicone oil were purchased from Sigma Aldrich (St. Louis, MO, USA). The polydimethylsiloxane and curing agent (Sylgard 184 silicon elastomer kit) was purchased from Dow Corning (MI, USA). 4-Methylumbelliferyl phosphate (4-MUP) liquid substrate was purchased from Millipore Sigma (St. Louis, USA). Human Glycan 1 (GPC-1) biotinylated antibody was purchased from R&D systems (MN, USA). Biotinylated anti-CD63, anti-vinculin, and anti-GPC-1 antibodies were purchased from Abcam (MA, USA). Anti-EpCAM antibody was purchased from Invitrogen (MA, USA) and anti-CD63 was purchased from BD Biosciences (NJ, USA). Anti-rabbit and anti-mouse HRP-conjugated IgG secondary antibodies were purchased from Cell Signaling Technology (MA, USA). Laemmli sample buffer, nonfat dry milk (NFDM), and ECL substrate kit were purchased from Bioworld (CA, USA). Dulbecco's Modified Eagle Medium (DMEM) and penicillin-streptomycin were purchased from Corning (NY, USA), and fetal bovine serum (FBS) was purchased from Gibco (NY, USA). Paclitaxel was purchased from Selleck Chemicals (TX, USA).

2.2. Device fabrication

A homogenous mixture of the curing agent and polydimethylsiloxane (PDMS, Sylgard 184, Dow Corning) base, with a weight ratio of 1:10, was prepared and degassed for 1 h using Scienceware[®] vacuum desiccator (Sigma Aldrich, USA) to eliminate air bubbles (Yadav et al., 2020). Subsequently, the PDMS was spin-coated onto a 50 \times 75 mm glass slide and left overnight for curing, forming a thin film of approximately 200 μ m. For the creation of the negative mold for the top channel, a 0.3 mm thick piece of KAPTON[®] Tape (McMaster-Carr, USA) was cut into the shape of a converging-diverging microchannel using a Graphtec Cutting Pro FC7000MK2-60 cutting machine. The tape was then affixed to a Petri dish. Then the PDMS was poured into the mold and degassed again to remove any trapped air bubbles using the desiccator, followed by overnight curing at 60 °C. After curing, a 1 mm biopsy punch was used to punch holes for the inlet and an outlet. Detailed descriptions of the

device assembly and experimental procedures are provided in the Supplementary Notes.

2.3. Image processing and data analysis

All fluorescence images were processed using a custom developed code. More details can be found in [Supplementary Fig. 2](#). GraphPad Prism has been used for graphical representation along with statistical analysis. Unless otherwise specified, all data used in this study are shown as mean \pm standard deviation.

3. Results and discussion

3.1. Membrane as microwells reactors

Utilizing Polycarbonate Track-Etched (PCTE) membranes, characterized by their uniform cylindrical pores ([Dutt et al., 2021](#); [Lin et al., 2019](#)) with minimal protein binding ([Supplementary Fig. 3](#)), the Mem-dELISA technology innovatively transforms these pores into microwells by selectively sealing one end (as depicted in [Fig. 1](#)). This transformation is achieved by first putting a 1x PBS drop on a glass slide spin-coated (1000 rpm, 2 min) with a thin film of PDMS, subsequently immersing the membrane to expel air through capillary action, thus ensuring bubble-free microwell formation upon adhesion to the PDMS layer (Supplementary Notes). A PDMS microchannel is then placed over the membrane, thus facilitating the introduction, and diffusion of various reagents into the microwells and ensuring the isolation of samples post-oil sealing, demonstrated by the successful segregation of microwells with a fluorescein solution ([Fig. 1B](#)). The critical step of wicking prior to membrane placement prevents air entrapment, a common issue when the sequence is reversed ([Fig. 1A](#)).

With the initial workflow finalized, we optimized the height of the PDMS-based microchannel to enable seamless sealing of fluorescein solution-filled microwells by oil ([Fig. 2A](#)). The study spanned both hydrophobic and hydrophilic membranes with microchannel heights varied from 100 to 1000 μm . Since the surface of the PCTE membrane is uneven, high shear is necessary to remove the remnant water layer present on the top of the membrane. For hydrophilic membranes, the layer of water could not be removed until the microchannel height was reduced to 100 μm . Even with this lowered channel height, many water islands were observed thus corrupting sample partitioning ([Fig. 2C](#)). For hydrophobic membranes, optimal sample partitioning was achieved by reducing the microchannel height to 300 μm and less, as evidenced by clear separation in picoliter reactors filled with a fluorescein solution ([Fig. 2B and D](#)). Z-stack confocal imaging was performed to orthogonally confirm the removal of all air bubbles within the microwells in the hydrophobic membrane as shown in [Fig. 2E](#). As we move in the z-direction, the microwells transition into focus and recede out of focus at 25 μm . The results indicate that the height of the cylindrical pores is around 20 μm which aligns closely to the manufacturer's specifications of 21 μm . Using these results, we estimate that the volume of one microwell is $\sim 0.4 \text{ pL}$ while the membrane has a well density of $4 \times 10^5 \text{ wells/cm}^2$.

3.2. Single-molecule assay for free-floating B- β G and B-ALP

In this study, we have selected beta-galactosidase and alkaline phosphatase as our two candidate enzymes for performing duplex enzymatic reactions within the same microwell. For duplex assay, it's important to test the enzyme cross-reactivity with their substrates ([Obayashi et al., 2015](#); [Ono et al., 2018](#)). Systematic testing identified the beta-galactosidase-RDG and alkaline phosphatase-4 MUP pairing as optimal, minimizing fluorescence crosstalk and inhibitory effects,

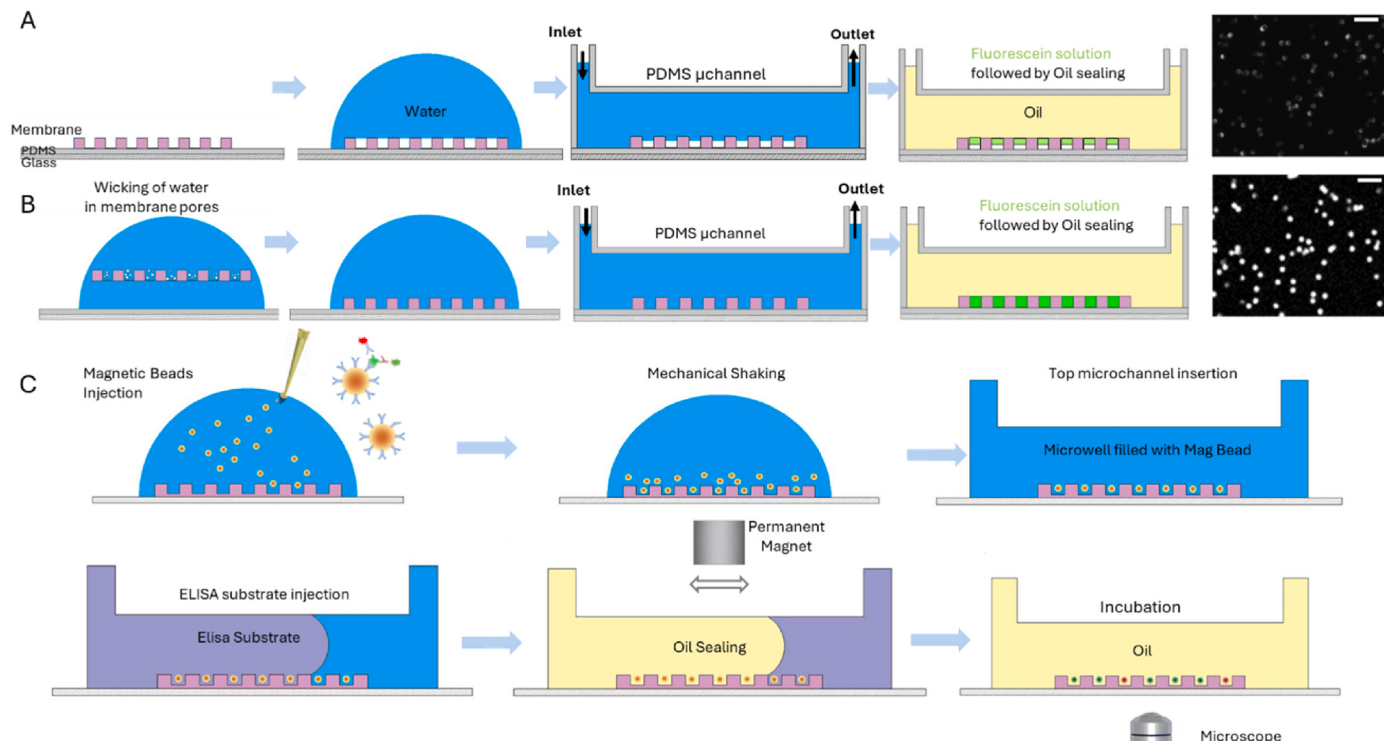


Fig. 1. Schematics of comparison of two workflows to use the through holes of the PCTE membrane to obtain microwells for digital assay. **A)** The membrane is first conformally sealed on the PDMS layer and then wetted with water. After inserting a PDMS micro channel from the top, fluorescein solution was inserted followed by oil sealing. The fluorescence images show trapped bubbles inside microwells. **B)** The membrane is first wetted with water to remove all trapped air bubbles due to wicking. Afterwards, the membrane is conformally assembled over the PDMS layer and a PDMS micro channel is inserted from the top. The fluorescence images obtained by first putting the fluorescein solution and then followed by oil sealing show the microwells are filled without trapped bubbles. Scale bar is 20 μm . **C)** Mem-dELISA device workflow for utilizing the through-holes of the membrane for digital ELISA.

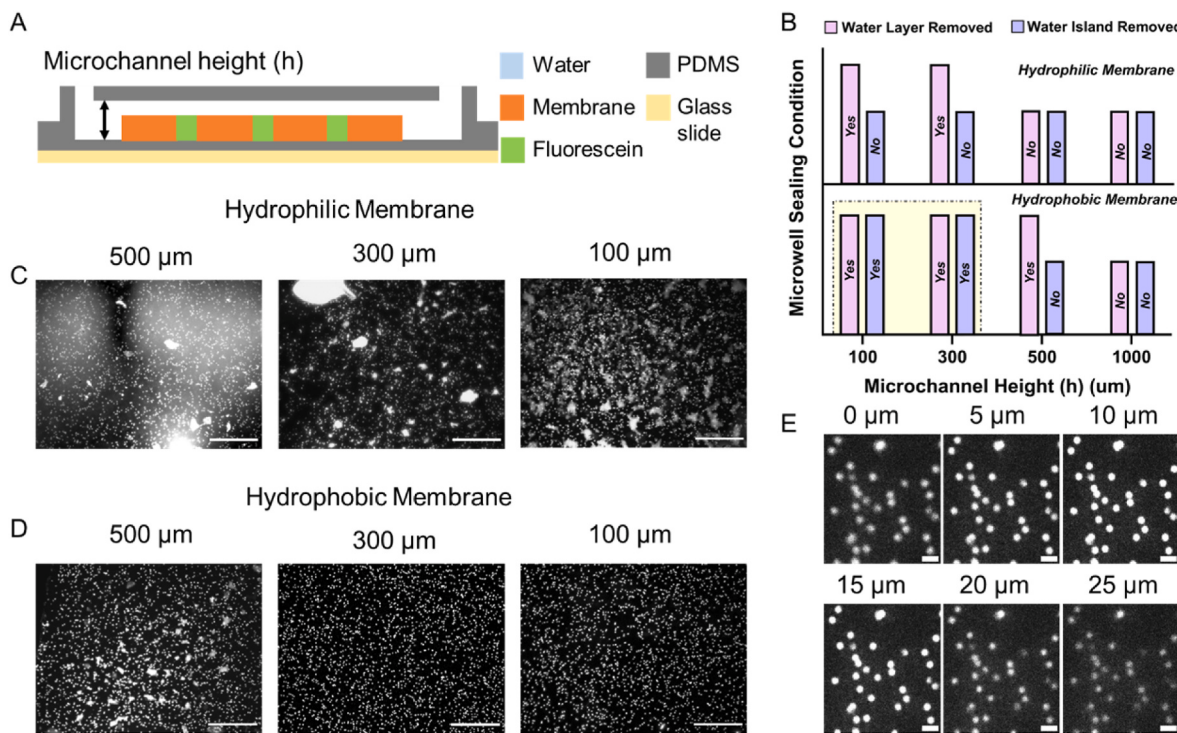


Fig. 2. Optimization of micro-channel height of Mem-dELISA device for perfect sealing of microwells. **A)** Schematics showing the height of the PDMS micro-channel used for injecting fluorescent liquid and oil for sealing of microwells. **B)** Graph depicting the parametric variation of micro-channel height to study its effect on the removal of fluorescent liquid by oil. The oil sealing method was very effective to remove the remnant water layer in hydrophobic membrane at a gap height of 300 μm and 100 μm . **C & D)** Images depicting the sealing of microwells by oil after filling them with fluorescent solution for both hydrophilic and hydrophobic PCTE membranes. **E)** Confocal z-stack images of microwells filled with 1 mM fluorescein solution and sealed with oil depicting no crosstalk between individual microwells. Scale bar is 200 μm for C) & D) and 10 μm in E).

detailed in [Supplementary Fig. 4](#). The B- β G reacts with RDG to give a red fluorescence signal (resorufin: Emission 584 nm) signal and B-ALP reacts with 4-MUP to give a blue fluorescence signal (methylumbellifereone: Emission 445 nm) that can be separated by using Rhodamine and DAPI filters respectively. We also performed a bulk cross-reactivity study in which the concentration of B- β G varied from 0 to 20 nM while keeping the B-ALP concentration fixed at 0.7 nM ([Supplementary Fig. 5](#)). The blue fluorescence remained roughly constant while the green fluorescence increased with the concentration of B- β G confirming minimum cross talk between the two enzymes.

After the successful demonstration of bubble-free partitioning of liquid into microwells, the Mem-dELISA platform was tested to study single molecule amplification of B- β G and B-ALP enzymes, as described in [Supplementary Fig. 6](#) and [Supplementary Notes](#). Time-lapse imaging ([Fig. 3A](#)) demonstrated the enzymatic reaction between B-ALP and 4-MUP substrate, with increasing fluorescence intensity over time. The intensity of each microwell at 25 min image was extracted using a custom-developed code, plotted as a histogram, and fitted with the sum of four Gaussian functions depicting the presence of 0, 1, 2, and 3+ enzymes in the microwells ([Fig. 3B](#)). Theoretically, the encapsulation of enzyme molecules in the empty microwells follows a Poisson distribution: $P(k : \lambda) = \frac{\lambda^k e^{-\lambda}}{k!}$. Here $P(k : \lambda)$ denotes the random probability of encapsulating k molecules in a microwell and λ is the average number of molecules per microwell. At the calculated lambda of 0.42, the expected probabilities of 0, 1, 2, and 3+ enzymes per microwell are 65.71%, 27.60%, 5.80%, and 0.01% respectively. The experimentally observed values obtained from Gaussian fitting matched well with the theoretical estimates from the Poisson distribution as shown in [Fig. 3C](#). The presence of discrete peaks is consistent with earlier reports ([Obayashi et al., 2015](#)). Similarly, we did the same experiment to study the enzymatic amplification of B- β G (30 pM) with its substrate (100 μM RDG). The sequential images revealed a temporal fluorescence increase ([Fig. 3D](#)).

Similarly, a histogram of the fluorescence intensity from each microwell from the 25-min timestamp image was generated and superimposed with the composite fit derived from the summation of four Gaussian functions ([Fig. 3E](#)). The obtained experimental values matched well with the theoretical estimates from the Poisson distribution with $\lambda = 0.224$ ([Fig. 3F](#)). The discrete fluorescence peaks observed with B- β G enzyme and RDG substrate reaction in microwells are also consistent with the previous literature reports ([Rondelez et al., 2005](#); [Sakakihara et al., 2010](#)).

We now proceeded to vary the concentrations of both B- β G and B-ALP in separate experiments within the range of 100–0.1 pM. With the sequential reduction in enzyme concentrations, the total number of wells lighting up decreased exponentially based on Poisson statistics as shown in the series of fluorescent images in [Fig. 3G](#) and I. A log-log plot revealing the percentage of fluorescent microwells as a function of the concentration is depicted in [Fig. 3H](#) and J. The biosensor had a working concentration range of 10–0.1 pM for both B- β G and B-ALP. This analysis shows that the Mem-dELISA methods and protocols have no effect on the biochemical reaction between different enzymes and their respective substrates.

After optimizing B- β G and B-ALP assays, a duplex assay with B- β G (30 pM) and B-ALP (100 pM) demonstrated co-encapsulation of proteins in microwells, indicated by merged green and red fluorescence (yielding yellow/orange color) in [Supplementary Fig. 7](#). The green and red hues correspond to the fluorescence signature of 4-MU and resorufin, respectively. Hence, a successful demonstration of the feasibility of dual-color digital enzyme assays is presented in this section and will be explored further in the upcoming sections.

3.3. Magnetic beads seeding optimization

To enhance the detection efficiency of Mem-dELISA platform, mag-

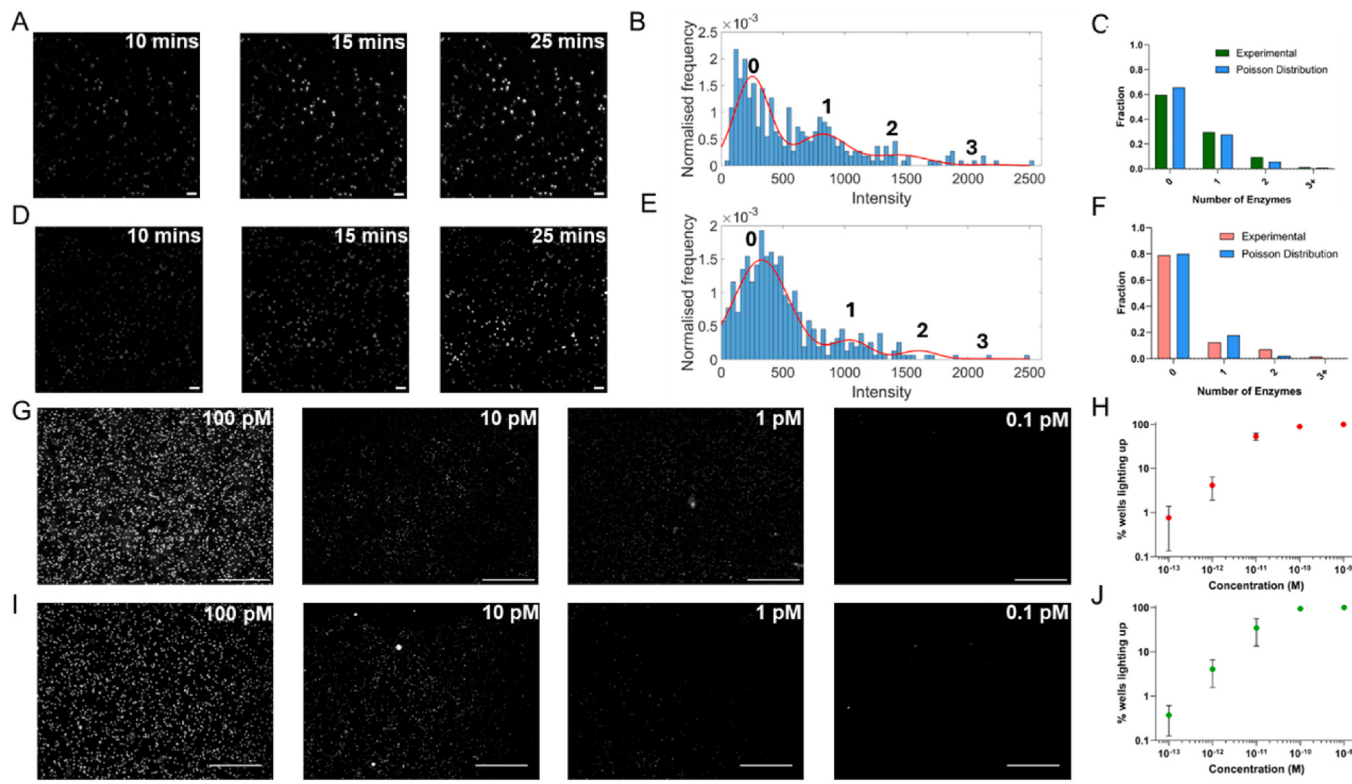


Fig. 3. Single molecule amplification results of B-ALP and B- β G in Mem-dELISA device. **A)** Sequential fluorescent images for digital enzymatic amplification for B-ALP at 10, 15 and 25 min. **B)** The intensity distribution of each microwell extracted from the 25 min image and fitted with sum of four gaussians corresponding to microwells having 0, 1, 2 and 3+ B-ALP molecules. **C)** Comparison of the % of microwells having 0, 1, 2 and 3+ B-ALP molecules obtained experimentally by gaussian fitting and obtained by Poisson's distribution having λ of 0.42. **D)** Temporal fluorescent images for digital enzymatic amplification for B- β G at 10, 15 and 25 min. **E)** The intensity distribution of each microwell extracted from the 25 min B- β G image and fitted with sum of four gaussians corresponding to microwells having 0, 1, 2 and 3 B- β G molecules. **F)** Comparison of the % of microwells having 0, 1, 2 and 3 B- β G molecules obtained experimentally by gaussian fitting and obtained by Poisson's distribution having λ of 0.224. **G)** Representative fluorescence images of serial concentration dilution (100 pM–0.1 pM) of B- β G. **H)** The corresponding log-log plot of the % active wells as a function of B- β G protein concentrations ($n = 3$). **I)** Illustrative fluorescence images of serial dilution in concentration (100 pM–0.1 pM) of B-ALP molecules and **J)** the corresponding plot of % active wells vs B-ALP concentration ($n = 3$). Scale bar is 50 μ m for A) & D) and 200 μ m in G) & I).

netic beads were employed to enhance protein molecule capture within microwells, addressing the limitation of diffusion-based methods (Lim and Zhang, 2007). However, the use of permanent magnets to direct beads into microwells quite often introduced the challenge of bead chain formation, adversely affecting seeding efficiency (Verbruggen et al., 2015). To develop more mechanistic insights into the system, COMSOL Multiphysics simulations of a permanent bar magnet were performed to understand the variation of magnetic flux density (Sharma et al., 2018) as a function of distance from the permanent magnet (Fig. 4A and Supplementary Fig. 8). The simulations show that the magnetic flux density varies as $\sim 1/r^3$ with r being the radial distance from the magnet (Fig. 4B). Moreover, the magnetic force exerted on the magnetic bead by the permanent magnet is directly proportional to the square of the gradient of the magnetic field. Hence, the simulations emphasized the necessity of optimizing the membrane-to-magnet distance to concentrate beads effectively without inducing chain formation.

The experimental results indicate the occurrence of large undesired magnetic bead chains when the beads were directly positioned atop the magnet (zone I, Fig. 4B). Further increase in the magnet-membrane distance led to a noticeable reduction in bead aggregation (zone II, Fig. 4B). Optimal reduction in bead chain formation occurred with the magnet placed 4 mm from the glass slide, establishing an effective magnet-membrane distance range between 4 mm and 1.6 cm, beyond which the force proved insufficient for attracting solution-phase beads onto the membrane. For all the experiments, the magnet was kept at 5 mm from the glass slide.

Preliminary experiments without a magnet at various magnetic bead

seeding densities showed less than 40% occupancy of microwells with a single bead (Fig. 4C and Supplementary Fig. 13) demonstrating that the allocation of magnetic beads into microwells adheres to the theoretical Poisson distribution limit of 37% (Chang et al., 2012). As the bead density increased to 10^8 beads/ml, single-bead occupancy decreased, and double-bead occupancy increased drastically. Hence, 2.4×10^7 beads/ml density was selected for further optimization using a magnet along with back and forth droplet movement to increase the bead capture in the microwells (Witters et al., 2013). After the beads settled on the membrane surface using the magnet, the Mem-dELISA chip was mechanically shaken for 15 min while keeping the magnet at a fixed position. Implementing mechanical agitation alongside magnetic influence significantly augmented single bead capture rates from $\sim 34\%$ to $>60\%$ (Fig. 4D), culminating in an enhancement of overall bead capture efficiency to surpass 80%. We provide a simple mechanistic explanation for enhanced bead capture efficiency. A simple force balance on a magnetic bead reveals that the viscous drag along with a small horizontal component of magnetic force acts in the x direction whereas the downward magnetic force along with gravity acts in the vertical direction (Sharma et al., 2018). This results in beads sliding on the membrane, increasing their chances of entering a microwell, whereas high surface tension prevents them from escaping. Also, during bead chain formation, the trapped particles amplify the magnetic field, thereby capturing additional particles atop them. Importantly, this enhanced field is limited to only a few bead diameters. Hence, well-separated and deep (beyond one particle diameter) microwells will prevent chain formation and improve sensitivity.

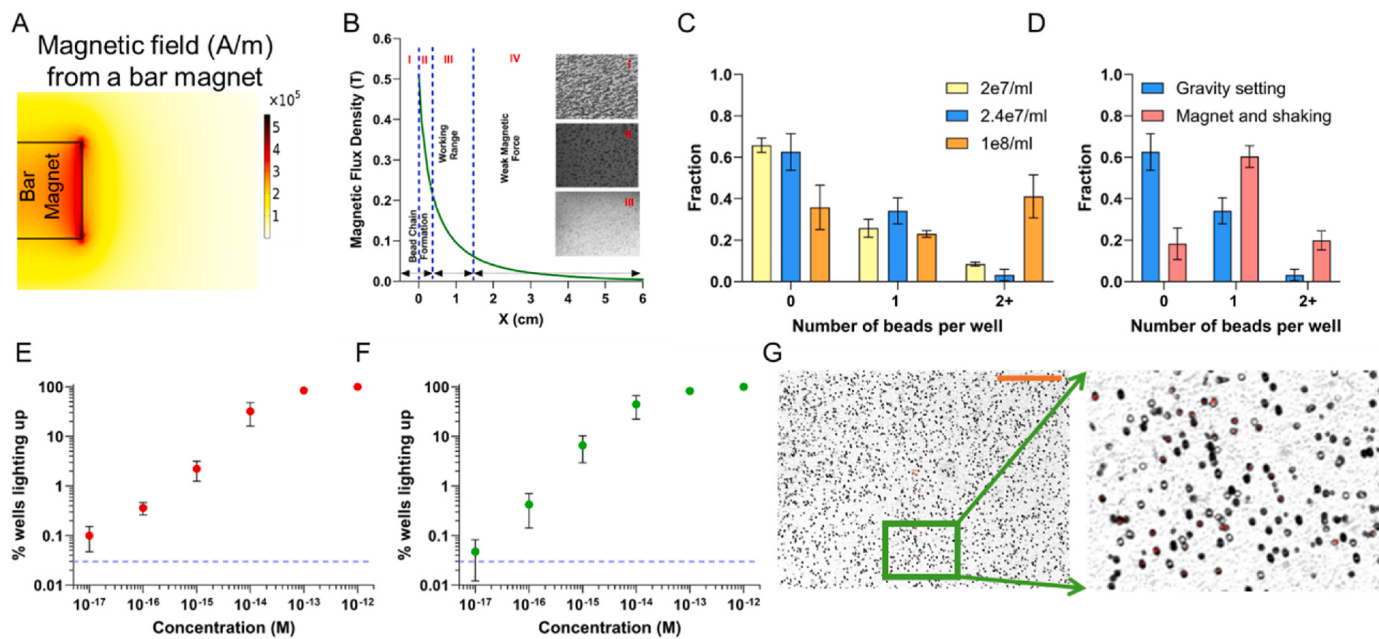


Fig. 4. Digital protein detection of B-ALP and B- β G protein molecules using magnetic beads in Mem-dELISA device. **A)** The surface plot of magnetic field from a permanent magnet obtained from COMSOL Multiphysics simulations. **B)** The variation of magnetic flux density (T) as a function of axial distance from the midpoint of the magnet obtained from FEM simulations. The experimentally obtained images of magnetic beads were obtained by varying the permanent magnet distance from the membrane surface. The bead phenotypes are divided into 3 zones. In I and II, magnetic beads chain formation was obtained which significantly reduces bead capture in the microwells. Regime III is the working range whereas in regime IV the magnetic force from the magnet didn't have any impact on the beads. **C)** The loading efficiency of magnetic beads in microwells (\sim half an hour incubation) without using a magnet for three different magnetic bead densities ($n = 3$). **D)** Comparison of magnetic beads loading in microwells with gravity settling and using a magnet with mechanical shaking for 15 min at bead density of 2.4×10^7 /ml ($n = 3$). **E) & F)** A log-log graph of % of fluorescent wells variation with B- β G and B-ALP protein concentration respectively ($n = 4$ minimum). **G)** The overlay of brightfield and red fluorescent image. The zoomed image depicts the active wells (red) and inactive wells. Scale bar is $200 \mu\text{m}$.

3.4. Magnetic bead-based multiplex assay

Following the optimization of the magnetic bead loading step, digital protein assays were conducted on the Mem-dELISA device to improve the limit of detection from Pico (10^{-12}) to 10 Atto (10^{-18}) molar range. For an initial test, 1 pM concentration of B- β G was incubated with streptavidin-coated magnetic beads with the hypothesis that each bead would capture at least one B- β G molecule. Empirical validation was obtained by overlaying the brightfield with corresponding fluorescence images at 50x resolution where all microwells that captured a bead showed fluorescence signal (Supplementary Fig. 9). Upon reducing the B- β G concentration to 20 fM, the analysis revealed that only a fraction of magnetic beads captured B- β G molecule as observed in the composite image obtained by overlaying both brightfield and fluorescence (red) images (Fig. 4G). The zoomed-in image shows the presence of empty microwells, microwells that contain a magnetic bead and are in an 'off' state, and microwells that contain a magnetic bead and are in an 'on' state (superimposed red color).

Now, the concentration of B- β G was systematically reduced by an order of magnitude from 1 pM to 10 aM as shown by the series of images in Supplementary Fig. 10A. Fig. 4E shows a log-log graph depicting the variation of % of fluorescent wells as a function of B- β G protein concentration. The dotted line is obtained from the negative controls, showing that 0.03% of microwells will be fluorescent. The calibration curve showed 5 logs of dynamic range (100 fM-10 aM) and a limit of detection of \sim 10 aM. It is important to note that the utilization of magnetic beads for capturing free-floating protein molecules has resulted in an improved limit of detection by 5 orders of magnitude, shifting from 100 fM to 10 aM as compared to cases without magnetic beads (Fig. 3H). Similarly, the concentration of B-ALP was also varied from 1 pM to 10 aM as shown in Supplementary Fig. 10B, and a similar calibration plot was made as discussed above in Fig. 4F.

Next, we tested the Mem-dELISA device to perform a duplex digital

protein assay by detecting both B- β G and B-ALP proteins simultaneously in a single experiment (Fig. 5A). Since the base substrates used in these reactions (RDG and 4-MUP) also produce a fluorescent signal, it was necessary to perform a negative control to obtain the baseline intensity. The intensities of all microwells were extracted from images (Fig. 5B) captured from both fluorescence filters (Blue and Red) and plotted as histograms as shown in Fig. 5C and D. As observed in negative controls, $<0.03\%$ of the microwells light up at an intensity threshold of five standard deviations from the mean value. Consequently, a microwell is designated as being in an 'on' state if its intensity exceeds this specified threshold. To perform the duplex digital assay, for the first experiment, 1 pM of B-ALP and 100 fM of B- β G were mixed and incubated with magnetic beads. As expected, at these concentrations, the majority of microwells were in an 'on' state as shown in Fig. 5E. The concentration of both protein molecules was serially decreased by an order of magnitude in subsequent experiments and the results were shown as composite images in Fig. 5 (H, K, N & Q). As the concentration decreases by an order of magnitude, the number of microwells crossing the threshold intensity decreases as well for both B- β G and B-ALP. For efficient data visualization, the histogram of the intensity of microwells was plotted for all concentrations of B- β G and B-ALP in Fig. 5 (F, G, I, J, L, M, O, P, R & S). As the concentration of the protein molecules decreased, the histogram peaks shifted towards the left indicating that the number of microwells lighting up also decreased significantly. Additionally, the microwell intensity from each microwell was also extracted from a representative image and plotted as a function of the microwell ID for various concentrations in Supplementary Fig. 11 for better visualization of this trend. Furthermore, the capture of protein molecules by magnetic beads shall also obey Poisson's distribution as described in previous reports (Liu et al., 2018). For a duplex assay, since a single bead is present to capture two free-floating protein molecules, the combined probability of capturing both protein molecules on the same magnetic bead shall be the multiplication of two independent

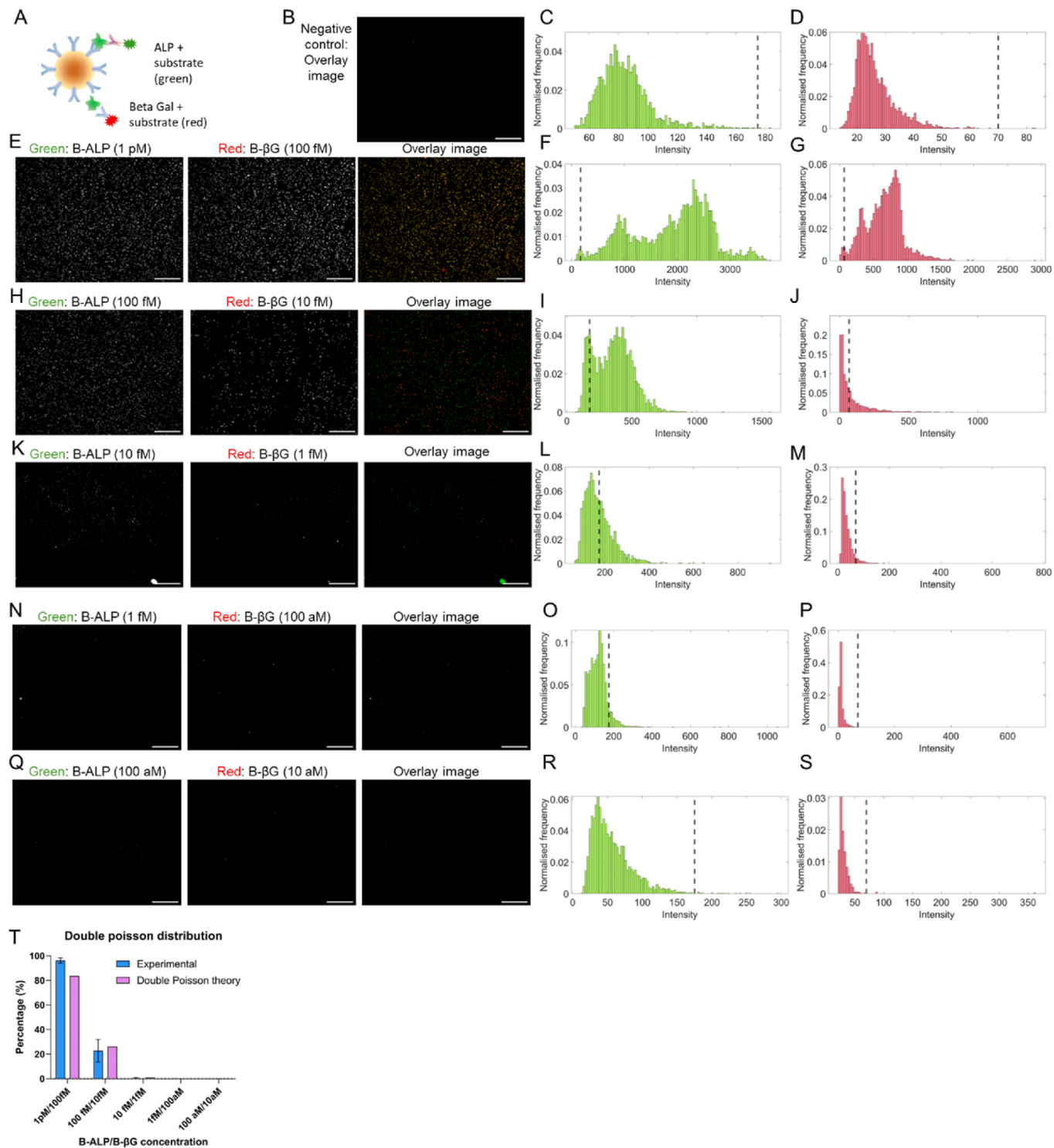


Fig. 5. Dual color protein detection using magnetic beads in Mem-dELISA device. **A)** Schematic of dual color protein detection. **B)** Overlay image of the negative control (mixture of 4-MUP (green color) and RDG (red color)). *Note that even though we look at blue fluorescence to observe ALP amplification, the image is shown in green color for better visualization of the overlay image*. **C & D)** Histogram of intensity distribution for negative control from both blue fluorescence and red fluorescence channels. The dotted line in both histograms represents the intensity value equal to mean + 5*standard deviation. **E, H, K, N & Q)** Fluorescence images from both filters along with the overlay image for the detection of B-ALP and B- β G simultaneously in the Mem-dELISA device. The concentrations of both B-ALP and B- β G proteins were serially diluted while keeping their ratio constant. The B-ALP concentration varied from 1 pM to 100 aM while B- β G concentration varied from 100 fM to 10 aM. **F, G, I, J, L, M, O, P, R & S)** Histograms of intensity distribution of microwells for both B-ALP (green bins) and B- β G (red bins) amplification in microwells with various concentration as mentioned in **E, H, K, N & Q**. The dotted line intensity was obtained from the negative control histogram. **T)** B-ALP and B- β G colocalization percentage and its comparison with double Poisson's statistics prediction at various concentrations, mentioned in **B, C, D, E, F**. Scale bar is 200 μ m for all images.

Poisson distributions. In Fig. 5T, the percentage of microwells having both B- β G and B-ALP proteins is plotted as a function of their concentrations which matches well with the theoretical predictions of double Poisson's distribution.

3.5. EVs based dELISA

EVs are an emerging class of promising highly heterogeneous circulating biomarkers that play important roles in shuttling molecular cargo from host cell to recipient cell, thereby facilitating intercellular communication, modulating drug resistances and immune response (Schwarzenbach and Gahan, 2020; Wills et al., 2021). Therefore, by first principles, alterations in the protein expression of EVs derived from tumors are expected to exhibit a strong correlation with the protein expression in the host tumor cells. In the case of breast cancer, the protein and gene expression of EVs has been associated with the prediction of therapy outcome and drug resistance (Ciravolo et al., 2012; Yu et al., 2016). Though the EVs heterogeneity in size and molecular cargo

has been well documented, bulk EV analysis methods (Dynamic Light Scattering, Nanoparticle Tracking Analysis, ELISA, and Western blots) have been predominantly used while advances have been made to perform single EV analysis using single-particle interferometric reflectance imaging with fluorescence, nanoparticle tracking analysis, microfluidic resistive pulse sensing, and nanoflow cytometry (Arab et al., 2021; Shao et al., 2018; Sharma et al., 2023).

Nonetheless, majority of single EV analysis platforms suffer from low dynamic range (~2 logs), interference from non-targets, and inherent issues with fluorescent probes such as protein autofluorescence and photobleaching (Ferguson et al., 2022; Mizenko et al., 2021; Shao et al., 2018). Instead of utilizing fluorescent probes, the developed dual-color Mem-dELISA biosensor utilizes enzymatic amplification for achieving higher signal to noise ratio. Moreover, the platform utilizes efficient wash protocols using a high ionic strength buffer (5X PBS) to minimize electrostatic interactions between non-targets and beads. The high throughput analysis of different surface proteins simultaneously on the surface of a single EV without EV lysis provides a holistic approach to

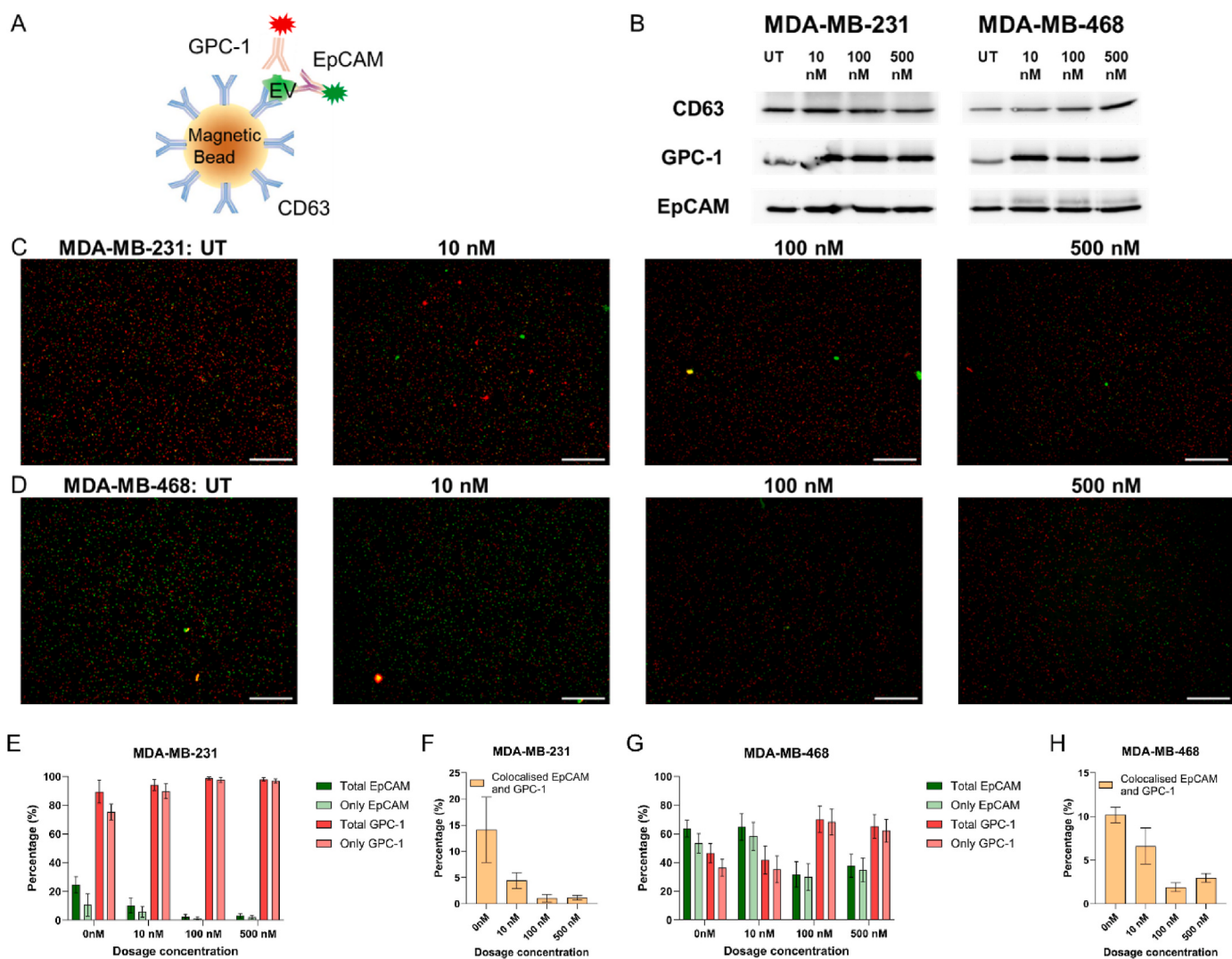


Fig. 6. Mem-dELISA device utilization for performing single EV assay to study the effect of Paclitaxel drug treatment on breast cancer cell lines. **A)** A schematic of the immunocomplex of EV sandwiched between CD63 coated magnetic beads and two reporter antibodies (EpCAM and GPC-1) conjugated with ALP and beta galactosidase enzyme respectively. **B)** Western blot images of CD63, GPC-1 and EpCAM proteins from cell lysate as function of drug concentration (10 nM, 100 nM and 500 nM) for MDA-MB-231 and MDA-MB-468 cell lines. **C & D)** Overlaid fluorescent images (red: GPC-1 and green: EpCAM) obtained from duplex digital ELISA of EVs as a function of drug dosage for both MDA-MB-231 and MDA-MB-468 cell lines, respectively. Left to right images represent untreated control, 10 nM, 100 nM and 500 nM Paclitaxel drug treatment. **E) & G)** Plot of % of EpCAM and GPC-1 protein content on EVs as function of drug concentration for MDA-MB-231 and MDA-MB-468 cell lines, respectively ($n = 3$). **F & H)** Graph showing the % of colocalized EVs (both EpCAM and GPC-1) as a function of drug concentration for MDA-MB-231 and MDA-MB-468 cell lines, respectively ($n = 3$). Scale bar is 200 μ m.

capture the heterogeneity with improved reproducibility to allow accurate diagnostic and therapeutic predictions. Multiple protein analysis on the same EVs improves the normalization of data with a reference protein to minimize experimental bias caused by upstream EV isolation steps (Sharma et al., 2023).

We utilized the multiplex Mem-dELISA platform to detect the two proteins colocalized on the surface of a single EV derived from cell culture media of breast cancer cell lines. As a proof-of-concept study, we studied the effect of chemotherapy (paclitaxel) treatment on two triple-negative breast cancer cell lines: MDA-MB-231 and MDA-MB-468 by quantifying the colocalization of GPC-1 and EpCAM proteins on the surface of EVs. Several reports suggest that both EpCAM and GPC-1 are biomarkers of breast cancer and are present in both MDA-MB-231 and MDA-MB-468 cell lines (Li et al., 2018; Lu et al., 2021; Matsuda et al., 2001). EpCAM has been attributed to increased drug resistance and poor prognosis (Soysal et al., 2013; Tian et al., 2021). We hypothesized that the normalized ratio of colocalized EpCAM-GPC-1 on EVs would provide insights on the effect of paclitaxel drug treatment on chemo-resistance for use in drug screening and therapy management.

Magnetic beads coated with CD63, a known tetraspanin marker, were selected to capture EVs isolated by ultracentrifugation from cell culture. An immunocomplex was formed where an EV is sandwiched between a CD63 capture antibody and enzyme coated GPC-1 and EpCAM detection antibody (Fig. 6A and Supplementary Notes). Capture antibodies were introduced serially while forming the immunocomplex followed by three times washes to minimize the cross-conjugation of enzymes and antibodies. The presence of GPC-1 and EpCAM in the cell lysate was confirmed by Western blot (Fig. 6B). For characterization of the effect of Paclitaxel drug treatment on the EVs derived from breast cancer cells, first, the cell lines were treated with different concentrations of paclitaxel (10 nM, 100 nM, and 500 nM). Following the drug treatment, the EVs were isolated from the cell culture media by ultracentrifugation. Fig. 1C shows the complete workflow of the Mem-dELISA platform for the duplex detection of GPC-1 and EpCAM proteins after immunocomplex formation. Fig. 6C and D shows a series of representative fluorescence images from both breast cancer cell lines to elucidate the effect of drug treatment on EVs for both MDA-MB-231 and MDA-MB-468 cell lines. Images from the left to right images represent the digital assay performed on EVs which were obtained from untreated control, 10 nM, 100 nM, and 500 nM Paclitaxel drug-treated cell lines. The red color corresponds to GPC-1 positive EVs while the green color corresponds to EpCAM positive EVs. The fraction of the EVs belonging to GPC-1 only, EPCAM only, and colocalized (both GPC-1 and EpCAM) is calculated based on set theory as shown in Supplementary Fig. 12. As shown in Fig. 6F and H, for both the breast cancer cell lines, as the concentration of paclitaxel was increased, the colocalized fraction of GPC-1 and EpCAM monotonically decreased. In contrast, the fraction of GPC-1 increases with an increase in drug treatment concentration (Fig. 6E and G). However, in the case of EpCAM alone, the fraction decreases monotonically with an increase of paclitaxel. These results suggest that the drug treatment suppresses the expression of EpCAM but not GPC-1. It also indicates that cancerous cells still exist and may require higher doses of chemotherapy to suppress the expression of GPC-1. Interestingly, this selective suppression cannot be identified by Western blot analysis of cell lysate as evident in Fig. 6B. This is likely due to the presence of dispersed soluble proteins in the cell culture media that generate false positive signals. This result suggests that our mem-dELISA EV colocalization assay provides more tumor state-relevant information than Western blot analysis of cell lysate.

4. Conclusion

In this report, we have presented the Mem-dELISA platform: a dual color, lithography-free, scalable, highly economical (< \$0.1 consumable cost) digital biosensor which integrated a piece of commercial PCTE membrane into a microfluidic channel to form thousands of microwells.

The facile integration of membrane into the microfluidics channels coupled with the wicking effect eliminated the need for expensive vacuum, fluidic pumps, or valves. For duplex color detection, two enzymatic amplification reactions namely beta-galactosidase and alkaline phosphate along with their selected substrates were individually optimized and subsequently performed simultaneously in the same experiment. Following the optimization of the bead loading efficiency to >80% through the introduction of a permanent magnet and mechanical shaking, the biosensor achieved a dynamic range of 1 pM–10 aM (5 logs) with a 10 aM limit of detection for B- β G and B-ALP proteins which is comparable (Supplementary Table S1) to commercial Simoa device and other reported digital protein detection platforms (Akama et al., 2019; Cohen et al., 2020; Wilson et al., 2016; Witters et al., 2013). Importantly, the use of membrane microwells that are open-ended on both sides allows loading of the solution with wicking, thus eliminates the need for expensive fabricated microwells and high-vacuum pumps for bubble removal in the current commercial platforms.

The Mem-dELISA platform was validated by performing digital ELISA of EVs extracted from two breast cancer cell lines after treatment with variable dosages of a chemotherapy drug. The colocalized fraction of EpCAM and GPC-1 protein pair and the EpCAM itself decreased with the drug dosage suggesting that these two ratios can be used as a surrogate marker for assessing therapy outcomes.

The Mem-dELISA device can be easily scaled to contain ~ 10⁶ wells (~ 2.5 cm² membrane) per chip, facilitating highly multiplexed operations when integrated with barcoded magnetic beads. Furthermore, augmenting ~10 membrane pieces per chip and establishing connections with the top microfluidics channel can empower the device to facilitate around 600 multiplexed assays (Song et al., 2021). For cancer detection, apart from EVs, the developed workflow can be applied to conduct colocalization assays on any multi-epitope-based antigens, such as viruses, lipoproteins, and ribonucleoproteins, among others. Beyond digital ELISA, we anticipate that this technology will find application in digital immuno-PCR for targeted drug delivery (Alipour et al., 2023), hybridization assays, single cell analysis, and colony formation assays.

CRediT authorship contribution statement

Himani Sharma: Writing – review & editing, Writing – original draft, Visualization, Validation, Software, Resources, Methodology, Investigation, Formal analysis, Data curation, Conceptualization. **Vivek Yadav:** Writing – review & editing, Writing – original draft, Visualization, Validation, Software, Methodology, Investigation, Formal analysis, Data curation, Conceptualization. **Alice Burchett:** Writing – review & editing, Resources, Investigation, Data curation. **Tiger Shi:** Writing – review & editing, Formal analysis. **Satyajyoti Senapati:** Writing – review & editing, Supervision, Project administration, Funding acquisition. **Meenal Datta:** Writing – review & editing, Supervision, Project administration, Funding acquisition. **Hsueh-Chia Chang:** Writing – review & editing, Supervision, Resources, Project administration, Funding acquisition, Conceptualization.

Declaration of competing interest

The authors declare the following financial interests/personal relationships which may be considered as potential competing interests:

Himani Sharma, Vivek Yadav, Satyajyoti Senapati and Hsueh-Chia Chang has patent #Application No 63/516,620 pending to University of Notre Dame du Lac. If there are other authors, they declare that they have no known competing financial interests or personal relationships that could have appeared to influence the work reported in this paper.

Acknowledgments

This work has been supported by the National Institute of Health

(NIH) Common Fund, through the Office of Strategic Coordination/Office of the NIH Director, 4UH3CA241684-03 (H.C.C. and S.S.), the National Cancer Institute grant K22CA258410 (M.D.), and the National Institute of General Medical Sciences grant R35GM151041 (M.D.). We thank the Datta lab members, Dr. Golnaz Asaadi Tehrani for her guidance regarding breast cancer chemotherapy studies, and Ms. R'ld Rumbach for technical assistance.

Appendix A. Supplementary data

Supplementary data to this article can be found online at <https://doi.org/10.1016/j.bios.2024.116848>.

Data availability

Data will be made available on request.

References

- Akama, K., Iwanaga, N., Yamawaki, K., Okuda, M., Jain, K., Ueno, H., Soga, N., Minagawa, Y., Noji, H., 2019. ACS Nano 13, 13116–13126.
- Alba-Bernal, A., Lavado-Valenzuela, R., Domínguez-Recio, M.E., Jiménez-Rodríguez, B., Queipo-Ortuño, M.I., Alba, E., Comino-Méndez, I., 2020. EBioMedicine 62. <https://doi.org/10.1016/j.ebiom.2020.103100>.
- Ali, N.S., Akudugu, J.M., Howell, R.W., 2019. World J. Nucl. Med. 18, 18–24.
- Alipour, M., Sheikhejad, R., Fouani, M.H., Bardania, H., Hosseinkhani, S., 2023. Biomed. Pharmacother. 166, 115299. <https://doi.org/10.1016/j.bioph.2023.115299>.
- Arab, T., Mallick, E.R., Huang, Y., Dong, L., Liao, Z., Zhao, Z., Gololobova, O., Smith, B., Haughey, N.J., Pienta, K.J., Slusher, B.S., Tarwater, P.M., Tosar, J.P., Zivkovic, A.M., Vreeland, W.N., Paulaitis, M.E., Witwer, K.W., 2021. Journal of Extracellular Vesicles, vol. 10, e12079. <https://doi.org/10.1002/jev2.12079>.
- Chang, L., Rissin, D.M., Fournier, D.R., Piech, T., Patel, P.P., Wilson, D.H., Duffy, D.C., 2012. J. Immunol. Methods 378, 102–115. <https://doi.org/10.1016/j.jim.2012.02.011>.
- Ciravolo, V., Huber, V., Ghedini, G.C., Venturelli, E., Bianchi, F., Campiglio, M., Morelli, D., Villa, A., Mina, P.D., Menard, S., Filipazzi, P., Rivoltini, L., Tagliabue, E., Pupa, S.M., 2012. J. Cell. Physiol. 227, 658–667. <https://doi.org/10.1002/jcp.22773>.
- Cohen, L., Cui, N., Cai, Y., Garden, P.M., Li, X., Weitz, D.A., Walt, D.R., 2020. ACS Nano 14, 9491–9501. <https://doi.org/10.1021/acsnano.0c02378>.
- Cohen, L., Walt, D.R., 2019. Chem. Rev. 119, 293–321. <https://doi.org/10.1021/crchemrev.8b00257>.
- Connal, S., Cameron, J.M., Sala, A., Brennan, P.M., Palmer, D.S., Palmer, J.D., Perlow, H., Baker, M.J., 2023. J. Transl. Med. 21, 118. <https://doi.org/10.1186/s12967-023-03960-8>.
- Dutt, S., Apel, P., Lizunov, N., Notthoff, C., Wen, Q., Trautmann, C., Mota-Santiago, P., Kirby, N., Kluth, P., 2021. J. Membr. Sci. 638, 119681. <https://doi.org/10.1016/j.memsci.2021.119681>.
- Ferguson, S., Yang, K.S., Zelga, P., Liss, A.S., Carlson, J.C., Del Castillo, C.F., Weissleder, R., 2022. Sci. Adv. 8, eabm3453.
- Hinestrosa, J.P., Kurzrock, R., Lewis, J.M., Schorck, N.J., Schroeder, G., Kamat, A.M., Lowy, A.M., Eskander, R.N., Perrera, O., Searson, D., Rastegar, K., Hughes, J.R., Ortiz, V., Clark, I., Balcer, H.I., Arakelyan, L., Turner, R., Billings, P.R., Adler, M.J., Lippman, S.M., Krishnan, R., 2022. Commun. Med. 2, 1–9. <https://doi.org/10.1038/s43856-022-00088-6>.
- Kelley, S.O., Mirkin, C.A., Walt, D.R., Ismagilov, R.F., Toner, M., Sargent, E.H., 2014. Nat. Nanotechnol. 9, 969–980.
- Kelly, K.M., Dean, J., Lee, S.-J., Comulada, W.S., 2010. Eur. Radiol. 20, 2557–2564. <https://doi.org/10.1007/s00330-010-1844-1>.
- Landegren, U., Hammond, M., 2021. Mol. Oncol. 15, 1715–1726. <https://doi.org/10.1002/1878-0261.12809>.
- Li, W., Shao, B., Liu, C., Wang, H., Zheng, W., Kong, W., Liu, X., Xu, G., Wang, C., Li, H., Zhu, L., Yang, Y., 2018. Small Methods 2, 1800122. <https://doi.org/10.1002/smtd.201800122>.
- Lim, C.T., Zhang, Y., 2007. Biosens. Bioelectron. 22, 1197–1204. <https://doi.org/10.1016/j.bios.2006.06.005>.
- Lin, X., Huang, X., Urmann, K., Xie, X., Hoffmann, M.R., 2019. ACS Sens. 4, 242–249.
- Liu, C., Xu, X., Li, B., Situ, B., Pan, W., Hu, Y., An, T., Yao, S., Zheng, L., 2018. Nano Lett. 18, 4226–4232. <https://doi.org/10.1021/acs.nanolett.8b01184>.
- Liu, X., Li, J., Cadilha, B.L., Markota, A., Voigt, C., Huang, Z., Lin, P.P., Wang, D.D., Dai, J., Kranz, G., Krandick, A., Libl, D., Zitzelsberger, H., Zagorski, I.,
- Braselmann, H., Pan, M., Zhu, S., Huang, Y., Niedermeyer, S., Reichel, C.A., Uhl, B., Briukhovetska, D., Suárez, J., Kobold, S., Gires, O., Wang, H., 2019. Sci. Adv. 5, <https://doi.org/10.1126/sciadv.aav4275> eaav4275.
- Lu, N., Zhang, M., Lu, L., Liu, Y.-Z., Zhang, H.-H., Liu, X.-D., 2021. Oncol. Rep. 45, 706–716. <https://doi.org/10.3892/or.2020.7880>.
- Matsuda, K., Maruyama, H., Guo, F., Kleeff, J., Itakura, J., Matsumoto, Y., Lander, A.D., Korc, M., 2001. Cancer Res. 61, 5562–5569.
- Mizenko, R.R., Brostoff, T., Rojalin, T., Koster, H.J., Swindell, H.S., Leiserowitz, G.S., Wang, A., Carney, R.P., 2021. J. Nanobiotechnol. 19, 250.
- Morasso, C., Ricciardi, A., Sproviero, D., Truffi, M., Albasi, S., Piccotti, F., Sottotetti, F., Mollica, L., Cereda, C., Sorrentino, L., Corsi, F., 2022. Breast Cancer Res. Treat. 192, 65–74. <https://doi.org/10.1007/s10549-021-06474-3>.
- Obayashi, Y., Iino, R., Noji, H., 2015. Analyst 140, 5065–5073. <https://doi.org/10.1039/C5AN00714C>.
- Ono, T., Ichiki, T., Noji, H., 2018. Analyst 143, 4923–4929. <https://doi.org/10.1039/C8AN01152D>.
- Rissin, D.M., Kan, C.W., Campbell, T.G., Howes, S.C., Fournier, D.R., Song, L., Piech, T., Patel, P.P., Chang, L., Rivnak, A.J., Ferrell, E.P., Randall, J.D., Provuncher, G.K., Walt, D.R., Duffy, D.C., 2010. Nat. Biotechnol. 28, 595–599. <https://doi.org/10.1038/nbt.1641>.
- Rissin, D.M., Kan, C.W., Song, L., Rivnak, A.J., Fishburn, M.W., Shao, Q., Piech, T., Ferrell, E.P., Meyer, R.E., Campbell, T.G., Fournier, D.R., Duffy, D.C., 2013. Lab Chip 13, 2902. <https://doi.org/10.1039/c3lc50416f>.
- Rivnak, A.J., Rissin, D.M., Kan, C.W., Song, L., Fishburn, M.W., Piech, T., Campbell, T.G., DuPont, D.R., Gardel, M., Sullivan, S., 2015. J. Immunol. Methods 424, 20–27.
- Roganovic, D., Djilas, D., Vujnovic, S., Pavic, D., Stojanov, D., 2015. Bosn J basic. Med. Sci. 15, 64–68. <https://doi.org/10.17305/bjbms.2015.616>.
- Rondelez, Y., Tresset, G., Tabata, K.V., Arata, H., Fujita, H., Takeuchi, S., Noji, H., 2005. Nat. Biotechnol. 23, 361–365. <https://doi.org/10.1038/nbt.1072>.
- Sakakihara, S., Araki, S., Iino, R., Noji, H., 2010. Lab Chip 10, 3355. <https://doi.org/10.1039/c0lc00062k>.
- Schwarzenbach, H., Gahan, P.B., 2020. Cancer Drug Resist. 3, 63–82. <https://doi.org/10.20517/cdr.2019.90>.
- Shao, H., Im, H., Castro, C.M., Breakefield, X., Weissleder, R., Lee, H., 2018. Chem. Rev. 118, 1917–1950. <https://doi.org/10.1021/acs.chemrev.7b00534>.
- Sharma, H., John, K., Gaddam, A., Navalcar, A., Maji, S.K., Agrawal, A., 2018. Sci. Rep. 8, 12717. <https://doi.org/10.1038/s41598-018-31274-z>.
- Sharma, H., Yadav, V., D'Souza-Schorey, C., Go, D.B., Senapati, S., Chang, H.-C., 2023. ACS Nano 17, 9388–9404. <https://doi.org/10.1021/acsnano.3c01340>.
- Shim, J., Ranasinghe, R.T., Smith, C.A., Ibrahim, S.M., Hollfelder, F., Huck, W.T.S., Klenner, D., Abell, C., 2013. ACS Nano 7, 5955–5964. <https://doi.org/10.1021/nm401661d>.
- Song, Y., Ye, Y., Su, S.-H., Stephens, A., Cai, T., Chung, M.-T., K Han, M., W Newstead, M., Yessayan, L., Frame, D., David Humes, H., H Singer, B., Kurabayashi, K., 2021. Lab Chip 21, 331–343. <https://doi.org/10.1039/DOLC00678E>.
- Soysal, S.D., Muenst, S., Barbie, T., Fleming, T., Gao, F., Spizzo, G., Oertli, D., Viehl, C.T., Obermann, E.C., Gillanders, W.E., 2013. Br. J. Cancer 108, 1480–1487. <https://doi.org/10.1038/bjc.2013.80>.
- Tian, F., Zhang, S., Liu, C., Han, Z., Liu, Yuan, Deng, J., Li, Y., Wu, X., Cai, L., Qin, L., Chen, Q., Yuan, Y., Liu, Y., Cong, Y., Ding, B., Jiang, Z., Sun, J., 2021. Nat. Commun. 12, 2536. <https://doi.org/10.1038/s41467-021-22913-7>.
- Verbruggen, B., Tóth, T., Cornaglia, M., Puers, R., Gijs, M.A.M., Lammertyn, J., 2015. Microfluid. Nanofluidics 18, 91–102. <https://doi.org/10.1007/s10404-014-1409-8>.
- Wei, P., Wu, F., Kang, B., Sun, X., Heskia, F., Pachot, A., Liang, J., Li, D., 2020. Journal of Extracellular Vesicles, vol. 9, 1809765. <https://doi.org/10.1080/20013078.2020.1809765>.
- Wills, C.A., Liu, X., Chen, L., Zhao, Y., Dower, C.M., Sundstrom, J., Wang, H.-G., 2021. Cancer Res. 81, 452–463. <https://doi.org/10.1158/0008-5472.CAN-20-1976>.
- Wilson, D.H., Rissin, D.M., Kan, C.W., Fournier, D.R., Piech, T., Campbell, T.G., Meyer, R. E., Fishburn, M.W., Cabrera, C., Patel, P.P., Frew, E., Chen, Y., Chang, L., Ferrell, E. P., von Einem, V., McGuigan, W., Reinhardt, M., Sayer, H., Vielsack, C., Duffy, D.C., 2016. J. Lab. Autom., vol. 21, pp. 533–547. <https://doi.org/10.1177/2211068215589580>.
- Witters, D., Kneze, K., Ceysens, F., Puers, R., Lammertyn, J., 2013. Lab Chip 13, 2047–2054. <https://doi.org/10.1039/C3LC50119A>.
- Wu, C., Dougan, T.J., Walt, D.R., 2022. ACS Nano 16, 1025–1035. <https://doi.org/10.1021/acsnano.1c08675>.
- Wu, C., Maley, A.M., Walt, D.R., 2020. Critical reviews. Clin. Lab. Sci. 57, 270–290. <https://doi.org/10.1080/10408363.2019.1700903>.
- Yadav, V., Chong, N., Ellis, B., Ren, X., Senapati, S., Chang, H.-C., Zorlutuna, P., 2020. Lab Chip 20, 4273–4284. <https://doi.org/10.1039/DOLC00809E>.
- Yu, S., Wei, Y., Xu, Y., Zhang, Y., Li, J., Zhang, J., 2016. Tumor Biol. 37, 2849–2861. <https://doi.org/10.1007/s13277-015-4683-5>.
- Zandi Shafagh, R., Decrop, D., Ven, K., Vanderbeke, A., Hanusa, R., Breukers, J., Pardon, G., Haraldsson, T., Lammertyn, J., van der Wijngaart, W., 2019. Microsyst. Nanoeng. 5, 25. <https://doi.org/10.1038/s41378-019-0065-2>.